

Determining the Effect of Diffuse X-ray Emission on Point Source Detection

Vera te Velde

under the direction of
Dr. Frederick Baganoff
MIT Center for Space Research

Research Science Institute
August 1, 2002

Abstract

The Chandra X-ray Observatory has been used multiple times since the telescope was launched into orbit in 1999 to view the central region of our galaxy, the Milky Way. The data from all of these observations have been compounded into a single image of the 40 parsecs (pc) surrounding Sagittarius A*, the compact radio source that is thought to mark the location of the supermassive black hole at the center of our galaxy. In this image, there is a diffuse cloud of background radiation over the entire area, as well as approximately 2400 X-ray point sources. The background radiation is created by non-uniform clouds of hot, ionized gas. Point sources on top of this radiation are more difficult to detect against the background light. We create an image of only the diffuse background emission in this region and simulate a grid of point-sources of known flux to add to the background. By observing how visibility of these sources changes with flux, we determine what fraction of the point sources is obscured by this diffuse radiation.

1 Introduction

The Chandra X-ray Observatory (Chandra) has been used twelve different times to look at the central region of our galaxy (see Appendix A, Table 1). The result of combining these data is an image of unprecedented detail of the inner forty parsecs of the dynamical center of the Milky Way. The following sections detail how this image was obtained and describe the types of objects visible in the field.

1.1 Instruments

Since the Chandra X-ray Observatory was launched in July of 1999, the astronomical community has enjoyed an amazing view into the depths of the X-ray universe, made possible by Chandra's unprecedented high-resolution imaging and spectroscopic capabilities over the wide energy range of 0.08 to 10 keV[10]. The primary tool used to collect the data analyzed in this study is the imaging detector of the Advanced CCD (Charged-Coupled Device) Imaging Spectrometer (ACIS-I), an array of four frontside-illuminated CCDs that view 17×17 arcminutes ($17' \times 17'$), with approximately 1 arcsecond ($1''$) spatial resolution and sensitivity to high-energy X-rays. These capabilities are crucial when viewing the extremely crowded region around Sagittarius A (Sgr A) through the high interstellar column density along that line of sight.

1.2 The Galactic Center

When ACIS was used to view the $17'$ square of the Galactic Center (GC) for approximately 600 ks, the resulting image (see Appendix D, Figure 1) shows a background of diffuse emission and approximately 2400 X-ray point sources located in the Galactic Center (GC), approximately 8.0 kpc from the sun. In the center is the Sgr A complex, housing the $2.6 \cdot 10^6 M_{\odot}$ (2.6 million solar mass) black hole at Sgr A*. The surrounding region is by far the brightest

diffuse source in the image, and is composed of extremely dense clusters of stars and clouds of hot ionized gases. Most X-ray radiation within 1.5" of Sgr A* is not stellar, but originates from matter accreting onto the super-massive black hole[2]. Farther out, the X-ray radiation originates from various types of X-ray binaries (see Section 1.3) and diffuse clouds of hot gas (see Section 1.4).

1.3 X-ray Point Sources

Chandra detected 2384 X-ray point sources in the 17' square field. Most are concentrated towards the center, partly because it is difficult to distinguish off-axis point sources on account of the larger point-spread function (PSF)¹. This number represents approximately a factor of 16 increase in the number of point sources detected in that field after a factor of 5 increase in exposure time (see Appendix A). The corresponding image obtained in 2001 contained 150 sources[2]. This new level in completeness of source detection makes possible more detailed studies of the effects of other factors on source visibility. The question we explore here is: how does the background radiation from diffuse gas in the GC affect X-ray point source visibility? Once this question has been answered, we can try to understand the nature of the many detected point sources, and to use this information to study the evolution of star formation in our galaxy.

Most X-ray point sources are X-ray binaries, systems in which a more massive compact object (i.e., white dwarf, neutron star, or black hole) and a less massive star orbit around each other. There are two main classes of X-ray binaries: Low-Mass X-ray Binaries (LMXBs) and High-Mass X-ray Binaries (HMXBs), corresponding to two mechanisms for accretion of matter onto the compact object. The difference depends on the mass of the secondary

¹The Chandra mirrors consist of four nested barrel-shaped structures of parabolic mirrors, followed by four similar sets of hyperbolic mirrors. X-rays ricochet off these surfaces to the focal point at the end of the barrel structure. The mirrors reflect X-rays effectively only at shallow ($\sim 1^\circ$) incidence angles; hence photons from sources at large field angles are spread out, creating a larger PSF.

star (the star that donates matter to the compact object). In both cases, X-ray radiation is powered by loss of gravitational energy of matter as it falls through the accretion disk surrounding the compact object.

In HMXB systems, the secondary star is a high-mass ($\gg 1 M_{\odot}$) star early in its evolutionary cycle (for instance, O or B type main-sequence stars) with a powerful stellar wind emitting outwards in all directions. This stellar wind is powerful enough for the small fraction that is captured by the compact object to power X-ray radiation through accretion.

In LMXBs, the secondary star is less massive ($< 1 M_{\odot}$) and has a weak stellar wind. It instead donates matter by evolving to the point where it expands past its Roche Lobe². The much higher-mass compact object gravitationally distorts the secondary star into a tear-drop shape. Mass flows off the secondary star's surface through the pointed end of the tear-drop (directed towards the compact object) through the inner Lagrangian point³, forming a stream of matter that then collides with the accretion disk around the compact object. Friction within the accretion disk transfers angular momentum outward, allowing gas to spiral inward. As the gas nears the event horizon of the black hole, it becomes progressively hotter, eventually reaching temperatures of order 10^7 K, allowing it to emit X-rays. Much more matter accretes onto the compact object LMXB systems, and the accretion disk is therefore much larger.

More classes of X-ray binaries become evident as the types of compact objects are taken into consideration. The three main types, in order of decreasing radius and increasing mass, are white dwarfs, neutron stars, and black holes. White dwarfs in white dwarf X-ray binaries, known as Cataclysmic Variables (CVs) are in fact so much larger that the decreased gravitational potential energy causes them to be extremely faint in X-rays relative to black

²The Roche Lobe of the donor is the surface outside of which matter rotating with the binary star system is no longer gravitationally bound to the donor.

³The inner Lagrangian Point, L1, occurs between two stars in a binary system where the gravitational spheres of influence (in this case, distorted from the normal spherical shape) of each cancel out.

hole and neutron star systems. This is because the luminosity, L , resulting from accretion of matter onto the compact object is equal to the rate at which gravitational energy, E , is released. If an object of mass M is accreting matter at the rate of dM/dt ,

$$L = \frac{dE}{dt} = \frac{GM(dM/dt)}{R}$$

where R is the radius of the compact object. Most energy is released approximately at its surface. It is then also possible to compare efficiency of energy generation through accretion for these three types of objects. Using Einstein's formula for the total energy contained in mass (m), $E = mc^2$, we can determine the fraction η of the total available energy that is released as light:

$$\eta = \frac{L}{dE/dt} = \frac{\frac{GM(dM/dt)}{R}}{\frac{dM}{dt}c^2} = \frac{GM}{Rc^2}$$

In this way it is possible to determine that neutron stars are approximately twice as efficient as black holes and between ten and one hundred times as efficient as white dwarfs[3] (see Appendix B, Table 2 for a comparison of properties of white dwarfs, neutron stars, and black holes).

Although a vast majority of the point sources in this image are X-ray binaries, as many as 300 could be simple stars early in the evolutionary cycle. Some, like our sun, emit X-rays powered by their own magnetic activity. Others occur in RS CVn binary systems. These are two main-sequence stars orbiting close enough to be rotationally locked (each rotates once per revolution). X-ray emission in these systems is also attributable to magnetic activity.

1.4 Diffuse Emission

Radio, infrared, and hard X-ray light are the wavelengths most suited for seeing to the center of the galaxy. In optical and ultraviolet bands, heavy dust and gas clouds obscure almost all light originating beyond our local vicinity in the outer Milky Way. The equivalent hydrogen

column density on the line of sight to the Chandra field of $N_H \approx 6 \cdot 10^{22} \text{ cm}^{-2}$, as well as the general tendency for X-rays to be less affected by light-scattering in dust[7] imply that the interstellar medium should be transparent to X-rays at energies greater than 2 keV. However, the bright, diffuse emission from clouds of hot interstellar gas is as bright as many point sources in the same line of sight, so point sources are difficult to distinguish from the background. It is the extent of this obscuring effect that this project analyzes.

The origin of this Diffuse X-ray Background (DXB) is a complex subject. The background observable in X-ray and ultraviolet bands consists of hot ionized gas at temperatures of 10^6 K or higher. These high temperatures make it one of the most energetic components of the interstellar medium. At higher X-ray energies, (2-10 keV), the DXB appears more isotropic than at energies below 2 keV. It occurs over the entire sky, but concentrates along the galactic plane. In most of the sky, the background originates extra-galactically, but at low galactic latitudes (i.e. the Chandra image used in this study), a majority of the DXB observed is composed of coronal gases in the GC, heated by supernovae occurring approximately once per century[9]. Along with hot ionized gas, a small fraction of the DXB could originate from unresolved late type dwarf stars[5] and unresolved stars emitting X-rays powered by their magnetic fields. With Chandra's high level of source resolution, however, the fraction of the DXB from unresolved sources is minimized. The question of exactly how much influence unresolved sources still have on the DXB as seen by Chandra is a question of debate into which this research can provide insight.

2 Methods

This study started with a composite image of Chandra data from twelve different observations. The first phase of the project was to prepare this image for the source simulation experiment. This required identifying point sources, subtracting them from the original

image, and smoothing those areas to create an image representing the diffuse X-ray emission in the region. For this, the primary tool used was the *Chandra Interactive Analysis of Observations* (CIAO) data analysis software, designed for use on Chandra data⁴. The CIAO wavelet detection routine used for identifying point sources in the image was *wavdetect*, which correlates the image’s pixel values to a “Mexican Hat” wavelet function. Along with the *wavdetect* algorithm, the source detection program run on the original image also output a list of source regions, which are circles and ellipses defined around each source or filamentary structure. Therefore, the next step was to subtract these source regions from the data.

The raw data is stored in an events file, which is a list of every X-ray that hit the Chandra CCDs, along with information about each X-ray’s energy, location, and other qualities. Using this file, we can use CIAO’s *dmcoppy* tool to translate this events file into an image, or we can filter the image based on various characteristics. The data were first filtered based on energy, from 0.5 to 8 keV, to exclude cosmic ray and other particle-induced noise in that range. We then filtered based on location, by subtracting the events that occurred within each of the 2384 source regions found by *wavdetect*. This left an events file which, when viewed as an image, had black circles and ellipses where point sources actually were located (see Appendix D, Figure 2). When viewed this way, it was also apparent that some of the source region definitions only covered the center of the point source. To fix this, manual adjustments were made to the regions’ definitions, making them larger where necessary (see Appendix D, Figure 3). This was especially useful around the edges of the image, where the enlarged PSF in off-axis CCD locations caused the point source to blur into a larger disk than is typical of on-axis locations.

When all of these sources had been altered and re-subtracted from the image, it was

⁴For details on CIAO routines used in this research, see the CIAO home-page at the *Chandra X-ray Center* site at <http://cxc.harvard.edu/ciao/>.

then necessary to fill in the subtracted regions with interpolated values in order to create the finished image representing only the diffuse emission. The *dmfilth* command in CIAO can do this using several different pixel-value interpolation methods. Most, however, require background regions to be defined around each source for use in the calculation. The GLOBAL and BILINT methods are the two methods that do not require such definitions. GLOBAL simply uses the entire image as the background region, and the BILINT method uses only four nearby pixels for each interpolated pixel. We tested the GLOBAL and BILINT methods using a sub-image of the original image (in order to save calculation time). The BILINT method yielded smoothed source regions with unrealistic striations. The GLOBAL method, because it included the empty pixels at the edges of the image in the background region definition, created source regions that appeared much darker than the average brightness of the diffuse emission. Because it used the same background region for calculating every interpolated pixel, each smoothed source region was also almost always a different value than the surrounding area, so even with the pixels filled in, they were easily visible (see Appendix D, Figure 5).

The POISSON method did not show either of these problems or any other visible deviations from the true diffuse radiation (see Appendix D, Figure 6). This is because the POISSON actually mimics real-life X-ray event distribution when creating the interpolated values. It determines the mean count rate for the source region by the ratio of the total number of counts to the area of the background region, and places events randomly (i.e. according to poisson statistics) in the source region at that count rate. This creates a very realistic smoothed source region, and was therefore the method employed to smooth the image of all point sources. It was first necessary, however, to elaborate on CIAO-included routines in order to define the background regions required in the *dmfilth* parameter list. Two Perl scripts for similar tasks are already included in CIAO. The first simply defines the raw boundary of the background region by multiplying the radius or semi-major and semi-minor

axes by a user-defined factor. The second, however, is written on the assumption that each source region is secluded enough that no other source region falls within the corresponding background region's boundary. In this image, though, it was necessary to subtract both the original source region and all nearby source regions from each background region. To accomplish that, we wrote a script that calculates the distance between the centers of every pair of background and source regions, and if it is less than the sum of the radii and/or semi-major axes, the source region is subtracted from that background region.

When this background region list was used as the *dmfilth* parameter, though, several memory problems became evident. First, CIAO claimed that the background region file contained four more sources than the source region file. All four regions that were counted twice by *dmfilth* were ellipses with background regions defined by a large ellipse with 28 or more smaller source regions subtracted from the area. When viewed on the screen, though, it was apparent that not so many source regions were necessarily within the larger ellipse. The Perl script for creating background regions had been written to ignore semi-minor axis and angle information for elliptical region definitions, normally of the format $\text{ellipse}(h, k, a, b, i)$ where h is the x coordinate of the center, k is the y coordinate of the center, a is the semi-major axis length, b is the semi-minor axis length, and i is the tilt angle. The algorithm instead treated any ellipse as a circle with radius a . It therefore identified many source regions as necessary to subtract from the large ellipse when they were not, and it was possible to manually edit these cases out to create a shorter region definition. The four regions, originally with 28, 30, 40, and 40 source regions subtracted from the large ellipse, then had 7, 20, 19, and 11 regions, respectively, subtracted. The other problem encountered was that the *dmfilth* command is seemingly unable to completely execute if the source list is too long. We ran a script that, given a bin size, will run *dmfilth* on that many sources at a time through the entire file. By setting the bin size to one, it is therefore also possible to isolate any individual source regions that *dmfilth* can't interpolate new values for. In that

way, this process identified three source regions that caused *dmfilth* to fail. A closer look showed that all three were identical sources, located on a pixel with zero counts (black), with a radius of 0.25 pixels. The cause of this source region is still unknown, but we were able to create new source and background region files without these three regions, and including a source region for a source next to the three false sources which was apparently missed by the detection algorithm (see Appendix D, Figure 7).

Now that an image representing only the background emission (see Appendix D, Figure 8) had been completed, we began the second phase of the project. This involved simulating sources, adding them to the background image, running the source detection algorithm on the resulting images, and calculating the fraction that were detected through the diffuse emission. The first step in source simulation was to find a basic flux level and spectrum at which to simulate the sources. By observing that the Log(N)-Log(S) distribution⁵ of the sources in the image begins to flatten out at around forty counts per source over the total exposure, we determined that this level represents the turning point where sources start to be lost from the data due to the background radiation. The Portable Interactive Multi-Mission Simulator⁶ (PIMMS) was used to find the corresponding flux of such a source. By specifying the output energy range as 0.5 to 8 keV, in analogy to our own filtering, and the spectrum as an absorbed power law model with $N_H = 6 \cdot 10^{22} \text{ cm}^{-2}$ and $\Gamma = 2$, (See next paragraph for a more detailed description of this model) PIMMS was able to calculate the observed flux necessary as $1.648 \cdot 10^{-15} \text{ ergs cm}^{-2} \text{ s}^{-1}$, or $2.2206 \cdot 10^{-7} \text{ photons cm}^{-2} \text{ s}^{-1}$.

The next step was to actually create a spectrum for our simulated sources. For this we used Xspec software to create a spectrum with the total flux equal to that output by PIMMS. As input into PIMMS, we defined it as an absorbed power law model, which combines a

⁵A Log(N)-Log(S) distribution relates flux, S, to the number of objects, N, at or above that luminosity, with both axes on a log scale.

⁶PIMMS is freely available for online use at the Chandra Proposal Planning Toolkit web site at (<http://asc.harvard.edu/toolkit/pimms.jsp>).

photo-electric absorption function with the simple photon power law function. The simple photon power law is given by

$$A(E) = K(E/1 \text{ keV})^{-\Gamma},$$

where Γ is the photon index of the power law (dimensionless) and K is the number of photons $\text{keV}^{-1} \text{ cm}^{-2} \cdot \text{s}^{-1}$ at 1 keV. The photo-electric absorption function is given by

$$M(E) = \exp(-N_H \sigma(E)),$$

where N_H is the equivalent hydrogen column in units of $10^{22} \text{ atoms/cm}^2$ and $\sigma(E)$ parameterizes the photo-electric cross-section of common interstellar atoms, not including Thomson scattering[1]. When the expressions for $M(E)$ and $A(E)$ are multiplied, the result is an equation describing the number of photons incident on the mirrors at a given energy. Using the input parameters for N_H , Γ , and K , Xspec used this relationship to create a file of data points from the graph of photon energy verses photon number, which was then truncated to only include energy levels from .5 to 8 keV (see Appendix D, Figures 9, 10, and 11).

The next step was to specify coordinates at which to create sources. For this we created a program to define a grid of n by n source regions on top of the full image. These regions were then used as input to the *Model of AXAF (Advanced X-Ray Astrophysics Facility) Response to X-rays* (MARX) software⁷, which creates event lists for point sources of specified flux, spectrum, and location as a Chandra detector would see it. In order to run the MARX simulation 441 (using $n = 21$) times, we wrote another program that uses MARX to create

⁷For details on MARX, please see the *MARX 3.0 Technical Manual* web-page at (<http://space.mit.edu/CXC/MARX/manual/manual.html>).

individual point sources in events file format, converts them to image format, and adds them together into a single image (see Appendix D, Figure 12). When added to the background image (see Appendix D, Figure 13), it was then possible run the source detection algorithm in order to see how many simulated sources of each flux level were visible through the diffuse emission.

One other complication needed to be resolved before running the source detection algorithm. In the center of the image, the simulated sources are small and focused, while on the edges, the off-axis angle makes X-rays more difficult to focus, so point sources appear as disks. The source detection algorithm therefore needs to look for larger objects with increasing off-axis angle. The source size *wavdetect* looks for is set in the parameters in pixel values, but simply looking for a wider range of sizes causes large features in the diffuse emission in the center of the image to be detected. To avoid this, we created three images from the original image of background emission. One is of the center-most region, 1024 by 1024 pixels large. The second covers four times as much area, but the pixel resolution is decreased by a factor of two (binned by two) in each direction, so it is also 1024 by 1024 pixels large. The last covers the entire area and is binned by four, so it is 636 by 637 pixels large. After running the source detection algorithm on all three images, it is possible to count all of the detected sources in the image binned by one, then count only the detected sources from the image binned by two that weren't identified in the first image, and likewise with the image binned by four. In this way, the most obviously false sources are eliminated while still searching through the entire size range necessary for detecting sources in all areas of the image.

When creating the image of diffuse emission for each of these three regions, it was apparent that the large bin factor of the most complete image made background regions in the most crowded central region impossible to define, so *dmfilth* was not able to completely fill in that section. However, because this region is covered by the two other images, the data

from the center region in the binned by four image is not needed.

Analogously, three images of each grid of simulated sources of a given flux, one of each size and bin factor, were created with the MARX source simulation program. These images were then added to the corresponding diffuse emission images to create the total images on which to run the source detection algorithm.

Running the source detection algorithm on each of these images created both a source file and a region file of all the detected sources. Since there were three of each of these files for each flux level, one for the image with each bin factor, it was first necessary to combine the three source files. This was done the same way as with the original image, using an *Interactive Data Language* (IDL) script that combined the three lists and removed the larger sources that were also detected in an image with a lower bin factor. Each resulting source file was then translated back into a region file, using a second IDL script, for further editing.

In the image of diffuse emission, many filamentary features exist which are seen as point sources by *wavdetect*. These source regions were removed from the original source list, and therefore were again detected in the images containing simulated sources. In order to purge the resulting list of detected sources of these false sources, the detection algorithm was also run on the image of just the diffuse emission as a control case. Two scripts were necessary to remove false sources from the region file of detected sources. The first eliminated all sources centered farther than ten pixels from the defined centers of the simulated sources. Additionally, it was possible for false sources to coincidentally be detected within this ten pixel radius, so we also compared the detected source list created by running the source detection algorithm on the background image to the region file list from the image with simulated sources, and removed any source whose center was within one pixel of the center of a source detected in the background. After removing sources in both of these categories, the final list of detected sources of that test flux level was created, and simply counting the number of entries allowed us to determine the fraction of simulated sources that were

detectable through the diffuse emission.

3 Results and Discussion

A total of 28 flux levels were considered. The results are summarized in Appendix C, Table 3. These data indicate that the list of 2384 sources is not complete. A naive interpretation of the original Log(N)-Log(S) distribution supposed that a majority of sources above forty counts were being detected in the field, but our results show that only 3.9 percent are detected. It is necessary to have an approximately thirteen times brighter source to be ninety percent confident of detecting it.

These data are well fit by a simple curve, which will in the future make adjusting a Log(N)-Log(S) distribution relatively straightforward. See Appendix D, Figure 14 for a graph of the results.

These data are useful for predicting the populations of X-ray binaries of various types based on estimates from Chandra observations. It is important to note that a significant fraction of the loss in point source detection efficiency has to do with the Observatory itself. At the edges of the image, the PSF is considerably larger, which of course spreads out the light from every source and makes it harder to detect. This means that the corrections to the Log(N)-Log(S) distribution will depend strongly on the field angle. If instead of point sources we wish to study the background radiation itself, it is still best to consider only on-axis data, where contamination from point sources is minimized. We have therefore also determined a flux versus detection relationship from the center image (the innermost 8.3' square) separately. These data are also summarized in Appendix C and Appendix D, Figure 15.

In the case of on-axis data, it is only necessary to have a flux approximately four times the 40 count level to be ninety percent confident of detecting the source. This indicates that

although the DXB still prevents source detection to a much greater extent than expected, a majority of the effect at off-axis angles is due to the enlarged PSF. It is important to note that the enlarged PSF is only a factor when background radiation is also present. As the field angle increases, point sources look more like background because the light is more spread out; however this only prevents them from being detected as point sources when there is a genuine background from which to be distinguished.

To apply these results to theoretical estimates of X-ray binary population-related properties, however, both the effect of the DXB itself and the larger off-axis PSF of the Chandra ACIS-I detector need to be accounted for. It is apparent from the information presented in Appendix B that the most easily detected X-ray sources are those of LMXBs with neutron star or black hole compact objects. Therefore, a higher fraction of CVs and HMXBs are not being detected, and assuming that a significant population of CVs and HMXBs exists, a Log(N)-Log(S) distribution corrected for missing sources would correspondingly be the distribution for a wider range of X-ray binaries types. The current Log(N)-Log(S) distribution has in any case a higher representation by black hole and neutron star LMXBs.

This new information on X-ray binary populations can also provide insight into a model of star formation in our galaxy. The fate of any evolved star depends on its initial mass. Measurements of the relative populations of white dwarfs, neutron stars, and black hole binaries therefore provide crucial information on the initial mass function for star formation throughout the history of the Milky Way. These types of compact objects are visible almost exclusively in X-ray binary systems, so studies of this kind are the only way to obtain measurements of their populations.

4 Conclusion

Our results show that the diffuse X-ray emission has a much larger effect on X-ray point source detection than previously thought. The Chandra ACIS-I detector, when observing a region with background radiation, loses significantly more source detection efficiency off-axis due to the larger PSF. LMXBs tend to be of higher luminosity, so a greater fraction of CVs and HMXBs are among the missing sources.

In the future, it is important to further study how the change in PSF size can influence estimates of the point source contribution to the DXB. We can also apply the relationship between source flux level and fraction detected to obtain a Log(N)-Log(S) distribution representing a wider cross section of X-ray binary types, and compare this to predictions from various models of galactic evolution and mass distribution. Performing similar analysis on images from different regions of the sky may also provide a means of determining the effect of individual components of the DXB on source detection.

5 Acknowledgments

First and foremost, I would like to express my sincere thanks to Dr. Frederick K. Baganoff for guiding me through every step of this project. I also greatly appreciate Dr. Mike Muno and Dr. Mark Bautz at the MIT Center for Space Research for their help and advice. I also thank my tutor, Dr. John Rickert, for his suggestions and guidance with this paper. Finally, I thank the Center for Excellence in Education and the Research Science Institute, particularly Ms. Joann DiGennaro and Dr. John Dell, for making such an outstanding opportunity as RSI available.

References

- [1] Arnaud, Keith and Ben Dorman: “Xspec: An X-Ray Spectral Fitting Package.” 25 June 2002. High Energy Astrophysics Science Archive Research Center. 11 July 2002. <http://heasarc.gsfc.nasa.gov/docs/xanadu/xspec/manual/manual.html>.
- [2] Baganoff, F. K. et al.: “Chandra X-ray Spectroscopic Imaging of Sgr A* and the Central Parsec of the Galaxy.” Submitted to *The Astrophysical Journal* 2 February 2001.
- [3] Charles, Philip A. and Frederick D. Seward: *Exploring the X-ray Universe*. New York: Cambridge University Press, 1995.
- [4] Grimm, H.-J., M. Gilfanov, and R. Sunyaev: “The Milky Way in X-rays for an Outside Observer: Log(N)-Log(S) and Luminosity Function of X-ray binaries from RXTE/ASM data.” *Astronomy & Astrophysics* manuscript no. paper 50, 19 June 2002.
- [5] Ottmann, R. and J.H.M.M. Schmitt: “The Contributions of RSCVn Systems to the Diffuse X-ray Background.” *Astronomy & Astrophysics* 256 (1992): 421-427.
- [6] Pfahl, Eric, Saul Rappaport, and Philipp Podsiadlowski: “On the Population of Wind-Accreting Neutron Stars in the Galaxy.” *The Astrophysical Journal* 571 (2002): L37-L40.
- [7] Predehl, P. and J.H.M.M. Schmitt: “X-raying the Interstellar Medium: ROSAT Observations of Dust Scattering Halos.” *Astronomy & Astrophysics* 293 (1995): 889-905.
- [8] Snowden, S.L.: “The Interstellar Medium and the Soft X-ray Background.” *MPE Report* 263 (February 1996): 299-306.
- [9] Valinia, Azita and Francis E. Marshall: “RXTE Measurement of the Diffuse X-ray Emission from the Galactic Ridge: Implications for the Energetics of the Interstellar Medium.” *The Astrophysical Journal* 505 (20 September 1998): 134-147.
- [10] Weisskopf, M. C. et al.: “An Overview of the Performance and Scientific Results from the *Chandra X-ray Observatory*.” *The Publications of the Astronomical Society of the Pacific* 114, Issue 791 (January 2002): 1-24.

A Information on Chandra observations of the GC:

ID	Type	Time	Start	Stop	Release
0242	GT01	46.5	21.9.1999	21.9.1999	3.11.2000
1561a	GT02	36.2	26.10.2000	27.10.2000	15.10.2002
1561b	GT02	13.7	14.7.2001	14.7.2001	15.10.2002
2951	GT03	12.5	19.2.2002	19.2.2002	22.2.2003
2952	GT03	12.0	23.3.2002	23.3.2002	29.3.2003
2953	GT03	11.9	19.4.2002	19.4.2002	25.4.2003
2954	GT03	12.6	7.5.2002	7.5.2002	13.5.2003
2943	G03	39.8	22.5.2002	23.5.2002	31.5.2003
3663	G03	39.7	24.5.2002	24.5.2002	30.5.2003
3392	G03	170.2	25.5.2002	27.5.2002	31.5.2003
3393	G03	161.4	28.5.2002	30.5.2002	5.6.2003
3665	G03	92.4	3.6.2002	4.6.2002	6.6.2003

Table 1: This table shows the Chandra observation ID numbers for each of the 12 observations used in this research, followed by the mission type, total good viewing time in kiloseconds, start date, stop date, and public release date (dates shown in day.month.year format). (See Section 1).

B Compact Objects in X-ray Binaries

Object Type	Radius (km)	Mass (M_{\odot})	η
Black Hole	5	>3	0.06-0.42
Neutron Star	15	1.4	0.1
White Dwarf	10000	<1	0.01-0.001

Table 2: A summary of the properties of three types of compact objects in X-ray binaries. η is GM/Rc^2 , which shows the relative efficiency of each object's accretion disk of turning matter into X-ray radiation (see Section 1.3). Note that although the black hole radius is smaller and mass is larger than for white dwarfs, black holes are less efficient at creating X-ray radiation because a significant amount of the energy conversion takes place within its event horizon, where it isn't visible.

C Summary of Results

Flux	Number	Fraction	Number (center)	Fraction (center)
0.25	3	.00680272	1	.00917431
0.5	6	.01360544	3	.02752293
0.75	10	.02267574	4	.03669724
1.0	17	.03854875	6	.05504587
1.5	39	.08843537	17	.15596330
2.0	66	.14965986	33	.30275229
2.5	96	.21768707	59	.54128440
3.0	137	.31065760	83	.76146789
3.5	162	.36734694	91	.83486239
4.0	185	.41950113	98	.89908256
4.5	210	.47619048	100	.91743119
5.0	235	.53287982	103	.94495413
6.0	271	.61451247	105	.96330275
7.0	308	.69841270	106	.97247706
8.0	336	.76190476	106	.97247706
9.0	355	.80498866	107	.97247706
10.0	367	.83219955	109	.98165137
11.0	377	.85487528	108	1.0000000
12.0	392	.88888889	108	.99082569
13.0	397	.90022676	107	.98165137
14.0	400	.90702948	109	1.0000000
15.0	409	.92743764	109	1.0000000
16.0	417	.94557823	109	1.0000000
17.0	418	.94784580	110	1.0091743
18.0	425	.96371882	110	1.0091743
19.0	425	.96371882	109	1.0000000
20.0	423	.95918367	109	1.0000000
21.0	428	.97052154	110	1.0091743

Table 3: A summary of results. The Flux column gives the multiple of the basic flux ($2.2206 \cdot 10^{-7}$ photons/cm/cm/s, as calculated by PIMMS) used in that test. The Number column gives the number of detected sources out of a total of 441 simulated sources, and the Fraction column gives the equivalent fraction of sources detected. The Number (center) and Fraction (center) columns give the corresponding information for the same analysis of only the central quarter of the image. A total of 109 sources were simulated in this region. *Wavdetect* detected 110 sources at several flux levels, when one source was defined with two source regions. (See Section 3).

D Figures

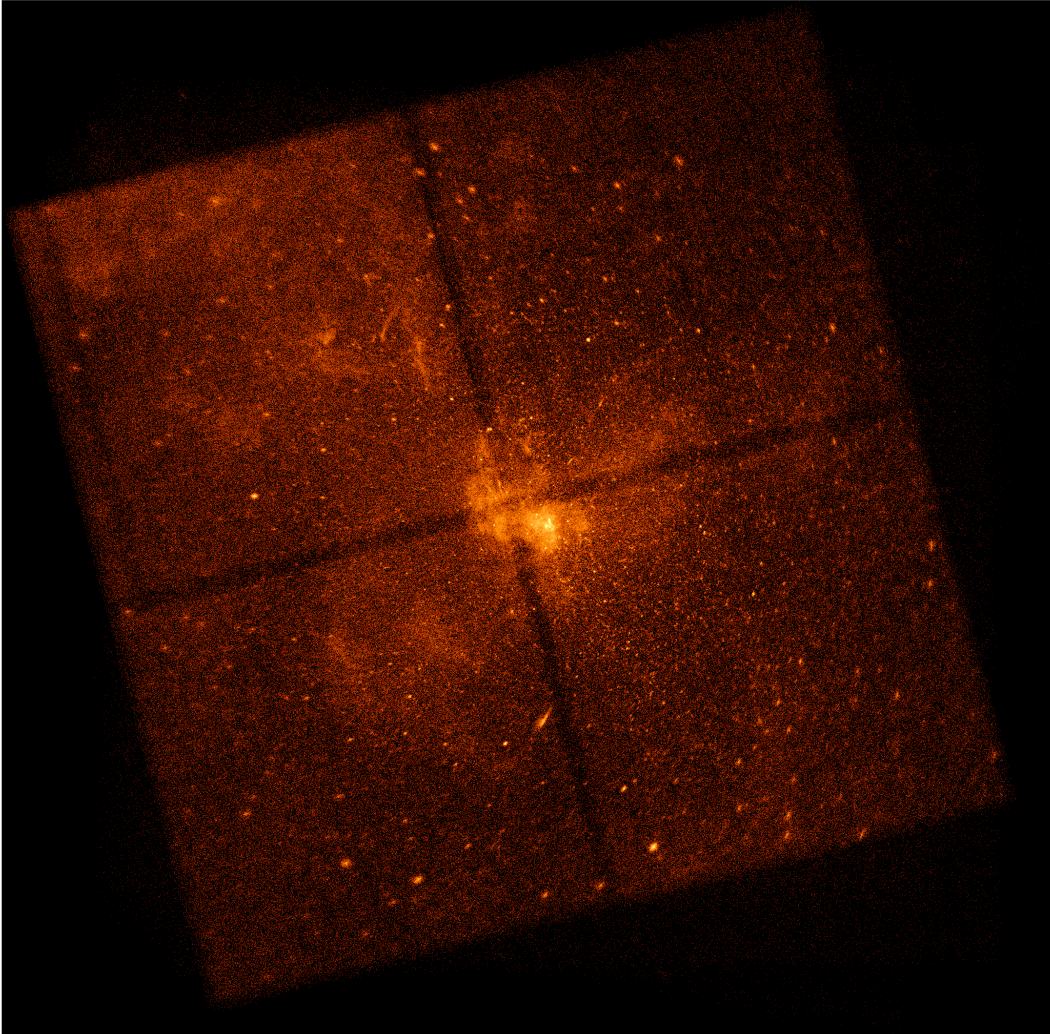


Figure 1: The central forty parsecs of the galaxy, as seen by Chandra. (See Section 1.2).

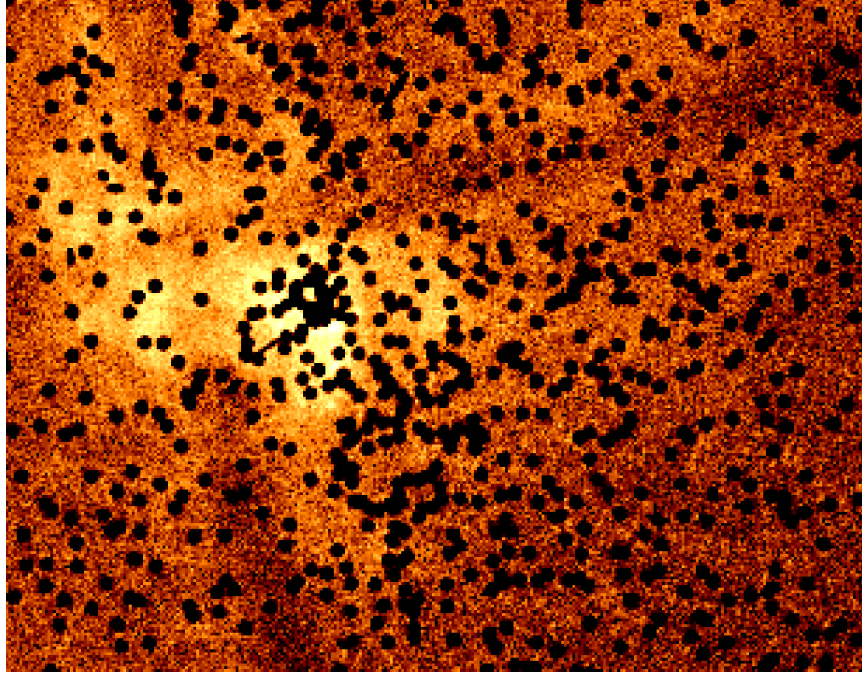


Figure 2: The central part of the image after filtering based on energy and subtracting source regions. (See Section 2).

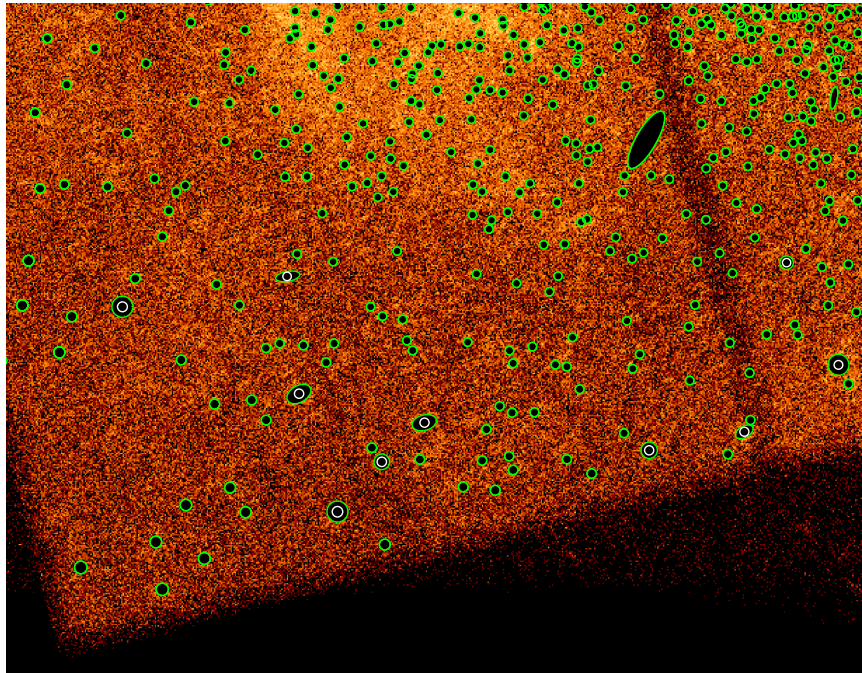


Figure 3: One corner of the image after filtering based on energy, subtracting source regions, and altering source regions that were originally too small as defined by the source detection algorithm. Altered source regions are shown in white; the final region list is shown in green. (See Section 2).

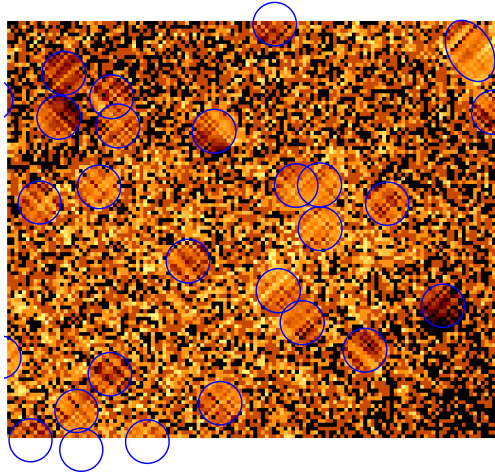


Figure 4: An example of a region smoothed by the *dmfilth* BILINT method. Note that original source regions, shown in blue, show unrealistic striations. (See Section 2).

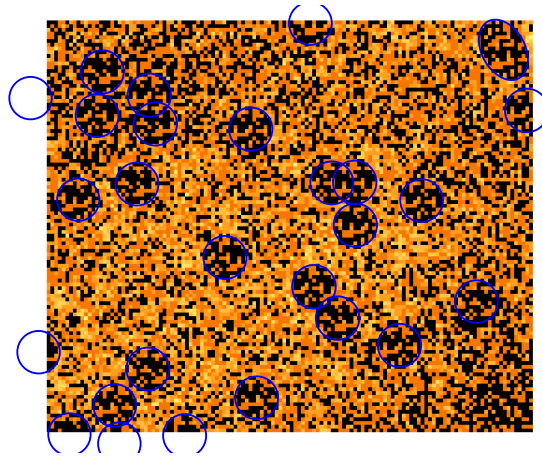


Figure 5: An example of a region smoothed by the *dmfilth* GLOBAL method. Note that original source regions, shown in blue, are visibly darker than the surrounding area. (See Section 2).

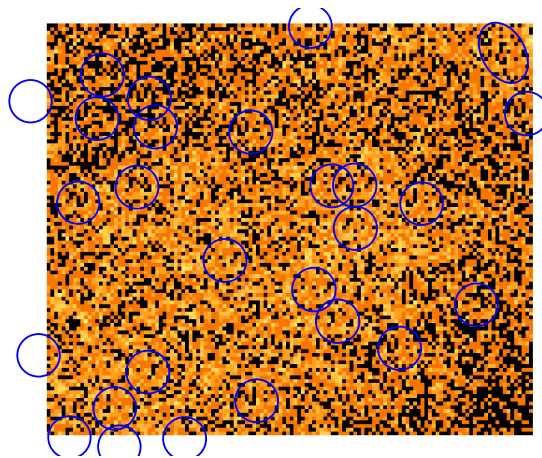


Figure 6: An example of a region smoothed by the *dmfilth* POISSON method. Source regions are shown in blue. (See Section 2).

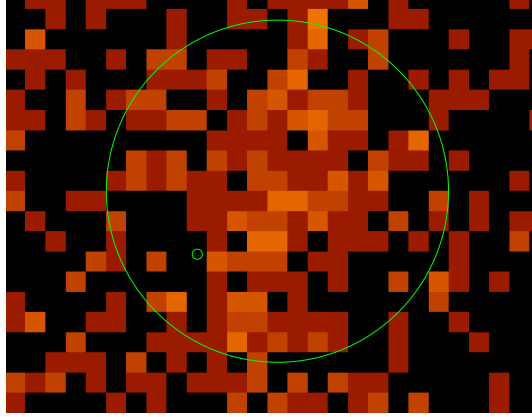


Figure 7: The small circle is the .25 radius region that was causing *dmfilth* to fail, and the large circle is the region that was missed by the detection algorithm. These two problems were possibly caused by the same thing; the source was actually detected where the small circle is but the region was defined incorrectly. (See Section 2).

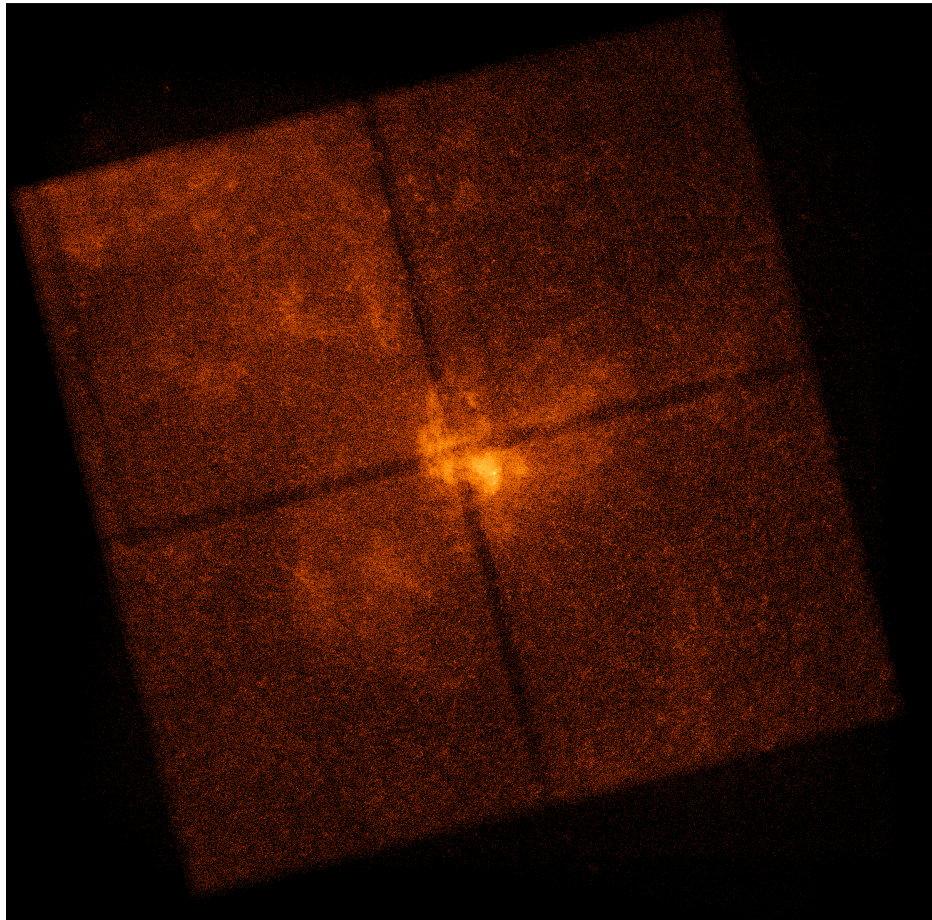


Figure 8: The Chandra image with all point sources smoothed over, creating an image representing only the background radiation. (See Section 2).

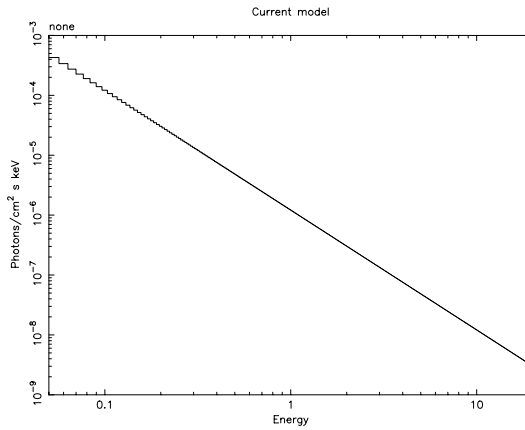


Figure 9: A power law model spectrum before absorption is taken into account. (See Section 2).

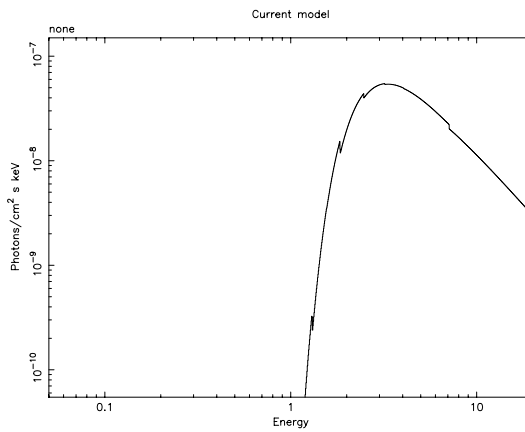


Figure 10: An absorbed power law model spectrum, simulated by XSPEC from 0.1 to 20.0 keV. (See Section 2).

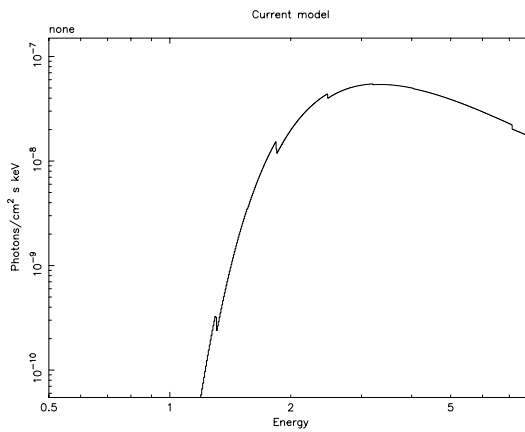


Figure 11: The same absorbed power law model spectrum as in Figure 10, after truncation to cover only the range from 0.5 to 8.0 keV, in order to match the image's filtering. (See Section 2).

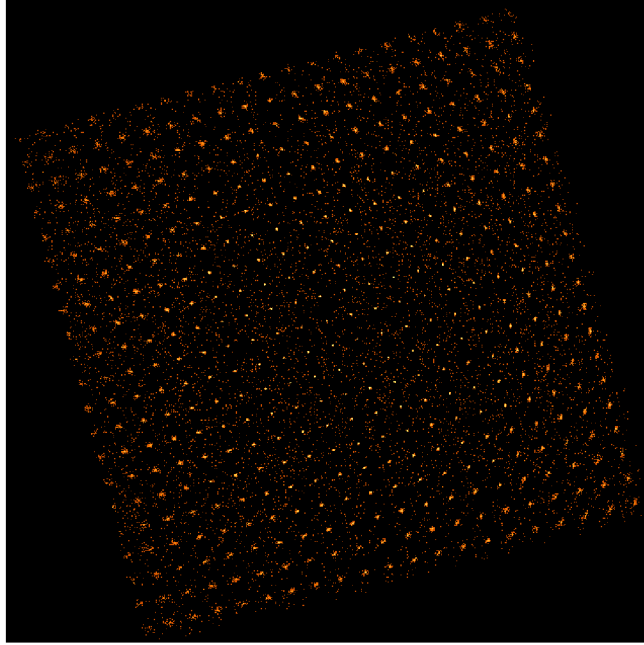


Figure 12: A grid of 441 simulated equal-flux point sources, created by MARX. (See Section 2).

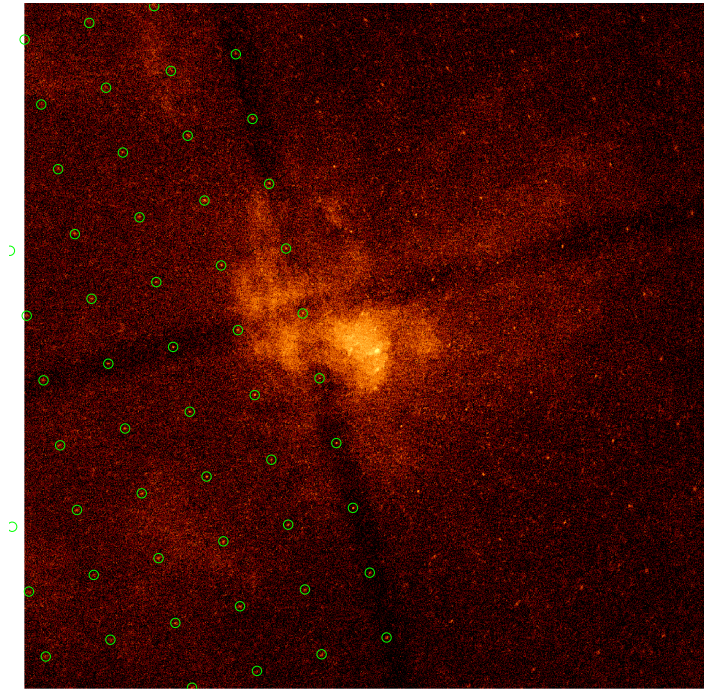


Figure 13: A grid of MARX-simulated sources added to the background image (central region). In order to show where the grid lies, the left half of the image shows the source regions in green. (See Section 2).

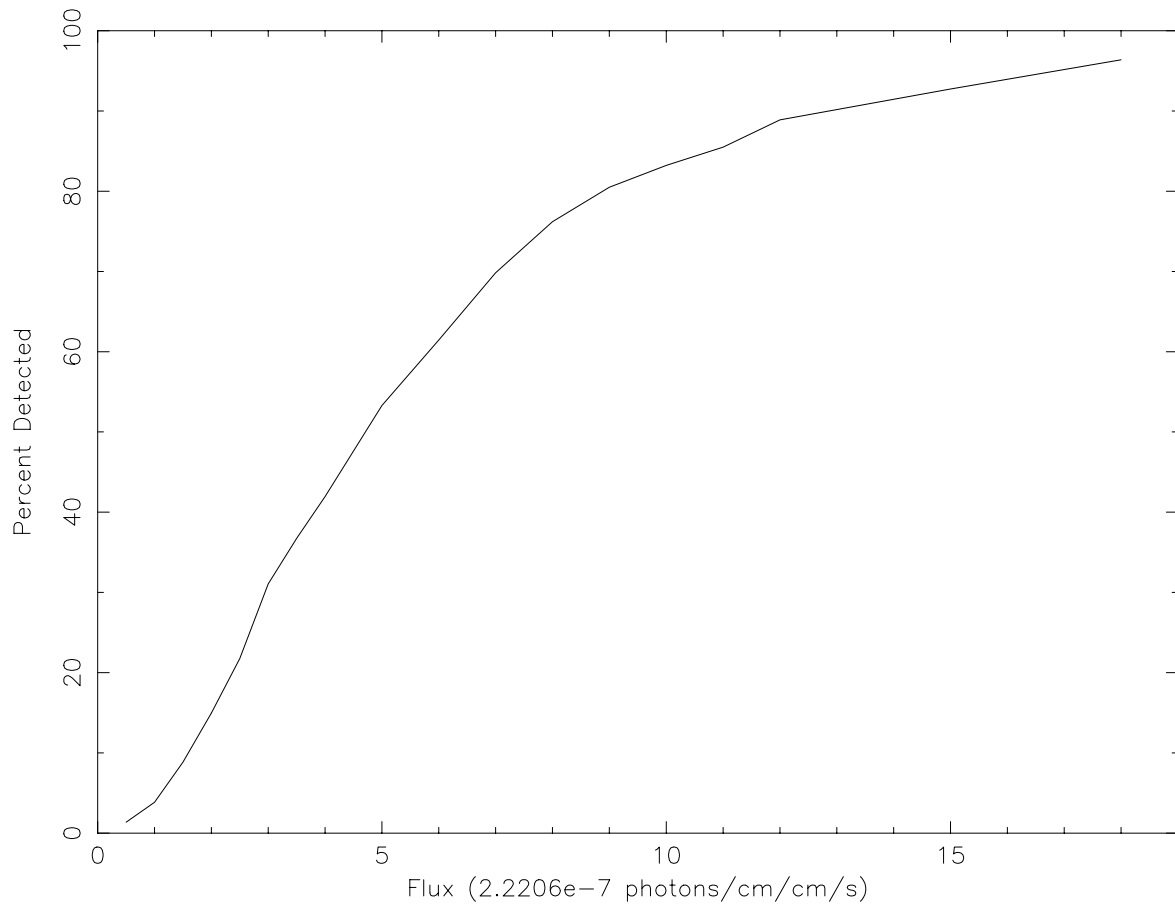


Figure 14: The graph of flux (given in multiples of the basic flux that yields forty total counts per source) versus percent detected. (See Section 3).

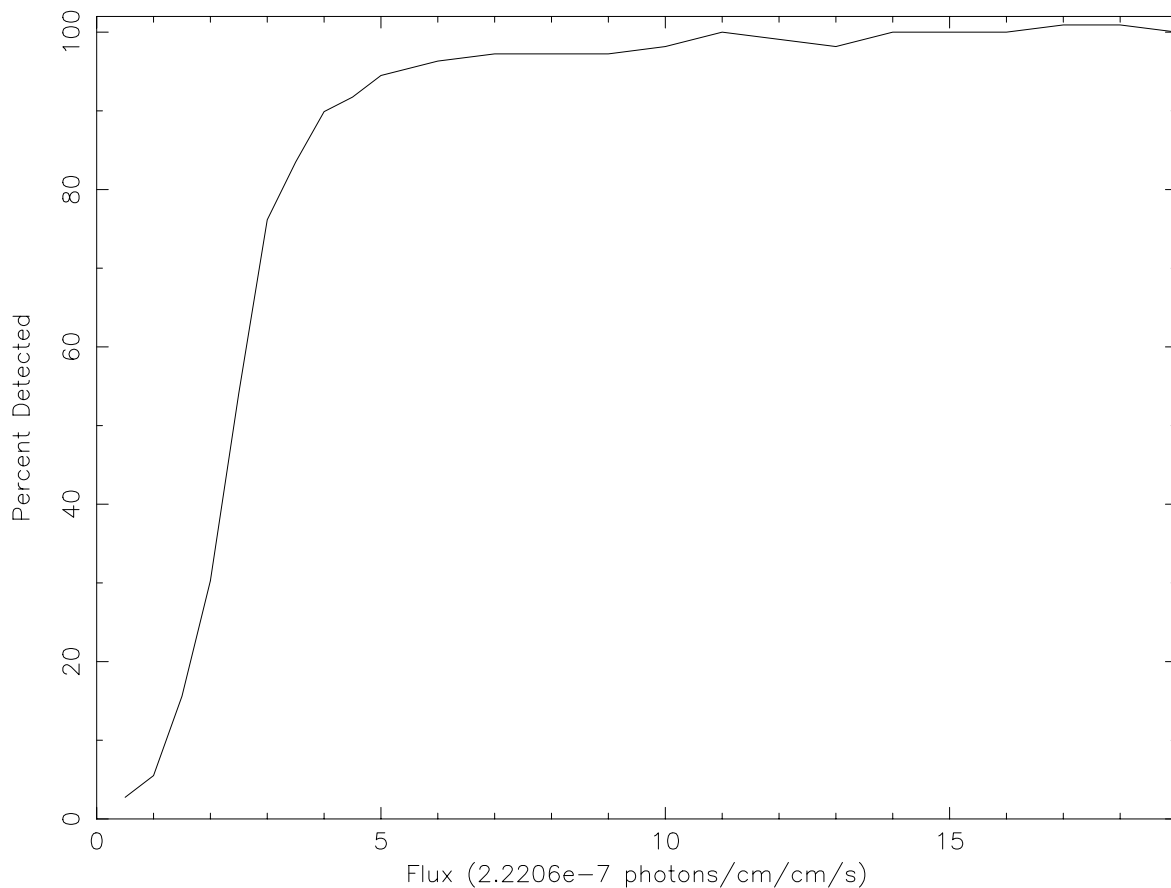


Figure 15: The graph of flux (given in multiples of the basic flux that yields forty total counts per source) versus percent detected in only the centermost quarter of the image. (See Section 3).